

# Digital Quantum Simulation of the Statistical Mechanics of a Frustrated Magnet

Jingfu Zhang,<sup>1,2,\*</sup> Man-Hong Yung,<sup>3,\*</sup> Raymond Laflamme,<sup>1,2,4</sup> Alán Aspuru-Guzik,<sup>3</sup> and Jonathan Baugh<sup>1,5,2</sup>

<sup>1</sup>*Institute for Quantum Computing, University of Waterloo, Waterloo, Ontario, N2L 3G1, Canada*

<sup>2</sup>*Department of Physics and Astronomy, University of Waterloo, Waterloo, Ontario, N2L 3G1, Canada*

<sup>3</sup>*Department of Chemistry and Chemical Biology,  
Harvard University, Cambridge, MA, 02138, USA*

<sup>4</sup>*Perimeter Institute for Theoretical Physics, Waterloo, Ontario, N2J 2W9, Canada*

<sup>5</sup>*Department of Chemistry, University of Waterloo, Waterloo, Ontario, N2L 3G1, Canada*

(Dated: June 6, 2012)

Many interesting problems in physics, chemistry, and computer science are equivalent to problems of interacting spins [1]. However, most of these problems require computational resources that are out of reach by classical computers. A promising solution to overcome this challenge is to exploit the laws of quantum mechanics to perform simulation [2]. Several “analog” quantum simulations of interacting spin systems have been realized experimentally [3–8]. However, relying on adiabatic techniques, these simulations are limited to preparing ground states only. Here we report the first experimental results on a “digital” quantum simulation on thermal states; we simulated a three-spin frustrated magnet, a building block of spin ice, with an NMR quantum information processor, and we are able to explore the phase diagram of the system at any simulated temperature and external field. These results serve as a guide for identifying the challenges for performing quantum simulation on physical systems at finite temperatures, and pave the way towards large scale experimental simulations of open quantum systems in condensed matter physics and chemistry.

The most challenging aspect of many-body simulation is that the memory and temporal resources often scale exponentially, rendering many problems of interest intractable by all known classical methods [2]. A promising solution is *quantum simulation*, in which a quantum system acts as a processor to simulate another physical system (quantum or classical). There are two classes of quantum simulation: “analog” simulators are typically engineered to simulate a particular class of Hamiltonians [9] and to find ground states of non-trivial Hamiltonians adiabatically, whereas “digital” simulators rely on universal quantum information processors (QIPs), capable of implementing a universal set of quantum gate operations [10] to simulate not only ground states, but also thermal states, and even time-evolving states.

Simulations of interacting spin systems are of particular importance to many applications, such as modeling magnetism [11], solving optimization problems [12], and restoring digital image [13]. Furthermore, understanding the properties of the spin models also offers insights to the computational complexity theory [14]. For example, the ground-state problem of the Ising spin model is known to be an NP-complete problem; this implies that if an efficient algorithm for solving the ground-state problem of the Ising model exists, then it can solve all other problems in the class of NP. This matter is related to the question whether P equals NP, and is a major unsolved problem in computer science.

In a series of recent experiments [3–6], based on the adiabatic methods, progresses of quantum simulation of various spin systems have been achieved in various physical systems. These experiments, however, suffers from two limitations: (a) they are limited to studying the ground-state properties only, and (b) the energy gaps

along the adiabatic paths must be large enough to avoid excitations from the ground states. In general, the energy gaps cannot be pre-determined efficiently, and are non-controllable. Therefore, the advantage of the adiabatic methods over classical methods is not guaranteed for all cases.

On the other hand, at finite temperatures, all of the thermodynamics of spin systems can be obtained by determining the partition function  $\mathcal{Z}$ , which, instead of NP, falls into a different complexity class called sharp-P, or #P. However, if an efficient algorithm for evaluating partition functions exists, then the ground-state properties of the corresponding spin systems can also be determined efficiently. Therefore, the problem of determining partition functions is at least as hard as the NP-problems, or simply called NP-hard.

Practically, partition functions cannot be computed efficiently, except for some simple cases such as 1-D spin chains. For classical spins, the classical Metropolis algorithm provide a means for generating the Gibbs distributions, through the construction of Markov chains with Monte-Carlo methods. For quantum systems, the quantum generalization of the Metropolis algorithm has been achieved [15, 16]. However, Markov-chain based methods, similar to the adiabatic methods, are limited to the cases where the Markov-matrix gaps cannot be too small to achieve convergence. Particularly, for frustrated spin systems, Metropolis sampling can result in ensembles trapped in local minima. In these cases, methods for direct encoding the Gibbs distribution into the states of the qubits would be more efficient. This is the key issue that motivates this experimental work.

By using a digital simulator, our system can explore the full phase diagram of the thermal state of the sys-

tem, as a function of temperature and magnetic field. All ranges are in principle accessible due to the digital nature of the simulation. Unlike other quantum phase transitions explored in other quantum simulation experiments [4–6], the underlying Hamiltonian of the simulator does not need to be restricted to certain types of interactions to be able to simulate the target system.

In this letter, we report the first digital quantum simulation of the finite-temperature properties a classical three-spin frustrated magnet, a building block of spin ice, (see Fig. 1), using a four-qubit quantum register based on NMR. The reason for simulating the frustrated magnet is that it exhibits a rich phase diagram of the total magnetization as a function of temperature and magnetic field. This allows us to experimentally probe various distinct features of this system. On the other hand, the phenomenon of geometric frustration is an interesting topic in condensed matter physics. For example, materials, such as water ice, exhibiting geometric frustration cannot be completely frozen; the motion at the molecular scale continues even at absolute zero. Recently, the same three-spin frustrated magnet at zero temperature has been simulated by trapped ions [5, 6]. We aim to make progress along this direction by extending the quantum simulation of the frustrated magnet to finite temperatures.

In our simulation, instead of a mixed state, the implemented algorithm prepares a coherent encoding of a classical thermal state (CETS) on a quantum register [17, 18],

$$|\Psi_\beta\rangle = \sum_k \sqrt{e^{-\beta E_k} / \mathcal{Z}} |\phi_k\rangle, \quad (1)$$

which is a pure state (a pseudopure state in the NMR experiment) with amplitudes  $\sqrt{e^{-\beta E_k} / \mathcal{Z}}$  equal to the square roots of the corresponding thermal state Gibbs distribution associated with the eigenstate  $|\phi_k\rangle$  of the Hamiltonian  $H$ . Here  $\beta = 1/T$  ( $k_B = 1$ ), and  $\mathcal{Z} = \text{Tr}(e^{-\beta H})$  is the partition function. The CETS, therefore, contains all of the information about the thermal density matrix

$$\rho_{th} = e^{-\beta H} / \mathcal{Z} \quad (2)$$

of the system. In fact, the thermal density matrix  $\rho_{th}$  can be directly obtained from the CETS state  $|\Psi_\beta\rangle$  by artificially “decohering” the off-diagonal elements of the density matrix  $|\Psi_\beta\rangle\langle\Psi_\beta|$  constructed from the CETS.

In this method [18], the number of quantum gates needed to prepare the CETS is linear in the number of spins for 1D cases and sub-exponential for 2D cases, but is still exponential in general for NP-problems. Nonetheless, the efficiency of this algorithm is independent of the simulated temperature, and not limited by the small-gap problem encountered in the Markov-Chain Monte Carlo algorithms. This makes it advantageous for simulating

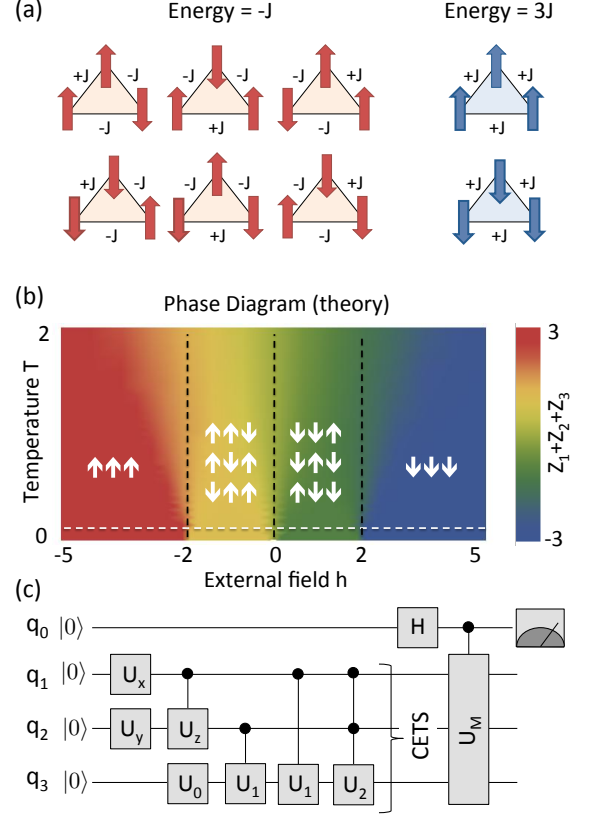


FIG. 1: Theoretical descriptions of the frustrated magnet. (a) All possible configurations of a three-spin frustrated magnet at zero temperature and zero magnetic field. There is a six-fold degeneracy in the ground state, leading to a non-zero entropy. (b) Theoretical phase diagram. The units of the axes are  $k_B$  and  $J$  for temperature and external field. The dashed line parallel  $h$ -axis denotes  $T = 1/11$ , which corresponds to the case of the experimental data taken in fig. 3. (c) Quantum circuit diagram for preparing and measuring the CETS  $|\Psi_\beta\rangle$  defined in Eq. 1 from the initial state  $|0000\rangle$ . The gate sequence for preparing the CETS on the lower three qubits is determined by the method in Ref. [18]. An explicit way for constructing the  $U_k$ -gates is given in the supplementary materials. The top qubit  $q_0$  serves as a probe for measuring the physical observables.

the low-temperature properties of frustrated spin systems. Furthermore, although this algorithm can at most yield a quadratic speedup for simulating the most general thermal states [18], the subclass of the CETS which can be created efficiently on a quantum computer can serve as a “heat bath” [19] for the simulation of the dynamics of open quantum systems, which could give an exponential advantage [20]. Our goal is to investigate how well such a CETS can be prepared in the laboratory subject to the existing experimental constraints.

In this experiment, three qubits encode the CETS of a triangle plaquette of Ising spins with equal couplings  $J$ , with temperature  $T$  and global magnetic field  $h$  as vari-

ables. A fourth ancilla qubit is used to probe the physical properties of the CETS by measuring the set of diagonal Pauli operators, so that quantities such as the total magnetizations and spin correlations can be extracted. These measurements are sufficient for determining the partition function  $\mathcal{Z}$ , from which any thermodynamic quantity of interest, e.g. entropy  $S$ , can be calculated.

To be more specific, the Hamiltonian of the frustrated magnet is defined by

$$H = J(Z_1 Z_2 + Z_2 Z_3 + Z_1 Z_3) + h(Z_1 + Z_2 + Z_3), \quad (3)$$

where  $Z_i \equiv \sigma_i^z$  is the  $\hat{z}$  Pauli matrix of the spin  $i$ . For  $J > 0$ , the coupling is antiferromagnetic, where the spins tend to minimize the energy by pointing in opposite directions. The external field  $h$ , however, tends to force the spins to align. The effect of finite temperature  $T$  is to wash out both tendencies. The competitions between these factors give rise to a phase diagram with a rich structure, as shown in Fig. 1b. For example, near some critical values of the external fields  $h = -2J, 0$  and  $2J$ , there are crossover points where the configuration of the spins, and hence the total magnetization, change abruptly. Near  $T = 0$  and  $h = 0$ , the ground state is fully frustrated with a six-fold degeneracy, as illustrated in Fig. 1a. This means that, unlike ordinary materials, the entropy (and hence heat capacity) of the frustrated spin system is non-zero at  $T = 0$ .

Our strategy for the study is as follows: for any given value of the temperature  $T$  and magnetic field  $h$ , the CETS  $|\Psi_\beta\rangle$  can be prepared with a quantum circuit of constant depth, as shown in Fig. 1c. Here we choose  $J$  as the unit for  $h$ . The three lower qubits,  $q_1, q_2$  and  $q_3$ , initialized into the  $|000\rangle$  state, are chosen as register qubits to encode the CETS. We choose the phase kick-back method [21] to extract information about the CETS by introducing a fourth qubit  $q_0$  as a probe qubit, shown as the top qubit in Fig. 1c. The probe qubit is then prepared in a superposition state  $(|0\rangle + |1\rangle)/\sqrt{2}$  and a controlled- $U_M$  gate operation is applied to the joint probe-CETS system to measure observables  $\langle U_M \rangle = \langle \Psi_\beta | U_M | \Psi_\beta \rangle$  on the top “probe” qubit. Here  $\langle U_M \rangle$  is proportional to the coherent element in the reduced density matrix of the probe qubit,

$$\rho_0 = \frac{1}{2} \begin{pmatrix} 1 & \langle U_M \rangle \\ \langle U_M \rangle^* & 1 \end{pmatrix}, \quad (4)$$

through tracing over the register qubits and can be extracted from the NMR signal of the probe qubit. By measuring the set of operators

$$U_M = \{Z_1, Z_2, Z_3, Z_1 Z_2, Z_2 Z_3, Z_1 Z_3, Z_1 Z_2 Z_3\}, \quad (5)$$

the full thermal state density matrix  $\rho_{th}$  can be reconstructed from the CETS.

For the NMR implementation, we choose as a sample of the  $^{13}\text{C}$ -labelled trans-crotonic acid dissolved in

d6-acetone, which forms a seven-qubit register; the four qubits in this experiment corresponds to the four carbon spins, and the other three nuclear spins are not directly involved after the preparation of the pseudopure state. The experiments were carried out on a Bruker DRX 700 MHz spectrometer. The structure of the molecule and the Hamiltonian parameters of the seven spin qubits are shown in Fig. 2a, where the NMR Hamiltonian of this system is given by

$$H_{NMR} = -\pi \sum_i \nu_i \sigma_i^z + \pi \sum_{k < l} J_{kl} \sigma_k^z \sigma_l^z / 2, \quad (6)$$

where  $\nu_i$  denotes the chemical shift of spin  $i$ , and  $J_{kl}$  denotes the coupling strength between spins  $k$  and  $l$ .

In the experiment, we exploit standard Isech and Hermite-shaped pulses to implement single-spin operations for the nuclei M and  $C_1$ - $C_4$ , and numerically optimized GRAPE pulses [23, 24] for manipulating  $H_1$  and  $H_2$  (for initial pseudopure state preparation only). A custom-built software compiler generates pulse sequences, including refocussing pulses, that are optimized for the highest unitary fidelity [24]. Furthermore, the radio-frequency (r.f.) spin selection techniques are exploited to improve the linewidth, and therefore the coherence, of the ensemble qubits [22, 25]. The effect of pulse errors due to r.f. inhomogeneity is reduced by a spatial selection of molecules in a region of high r.f. homogeneity. A labelled pseudo-pure state is prepared of the form  $\rho_s = \mathbf{00}\sigma_z\mathbf{0000}$  using methods described in Ref. [22], where  $\mathbf{0} \equiv |0\rangle\langle 0|$  and the order of qubits is as follows: M,  $H_1$ ,  $H_2$ ,  $C_1$ ,  $C_2$ ,  $C_3$ ,  $C_4$ . Note that we employ the deviation density matrix formalism [27].

The four carbon spins, initialized in the state  $\mathbf{0000}$ , are used to prepare and measure the CETS, where  $C_1$  is the probe qubit, and  $C_2$  -  $C_4$  are the register qubits for simulating the frustrated magnet. The CETS  $|\Psi_\beta\rangle$  is prepared by the pulse sequence shown in Fig. 2b. The NMR signal of  $C_1$  is acquired after the controlled- $U_M$  gate is applied. The controlled- $U_M$  is implemented by combining phase-flip and SWAP gate operations, and can be further be decomposed into nearest-neighbor coupling evolutions and single spin rotations. Fig. 2c illustrates the sequence for the observable  $Z_1 Z_2 Z_3$ .

As indicated in Eq. (4),  $\langle U_M \rangle$  is encoded in the coherent part of the probe qubit ( $C_1$ ) state. In the spectra of probe qubit (see supplementary material), the coherence is distributed among  $2^6 = 64$  peaks, each of which corresponds to a particular eigenstate of the remaining 6 qubits M,  $H_1$ ,  $H_2$ ,  $C_2$ - $C_4$ . The intensities of these peaks are obtained by a precise spectral fitting procedure [28]. In preparing and measuring the CETS, no computational operations are performed on the proton spins M,  $H_1$ , and  $H_2$ . The numerical simulations of the experiment take into account the effect of  $T_1$  relaxation process of the proton spins, which is experimentally measured though

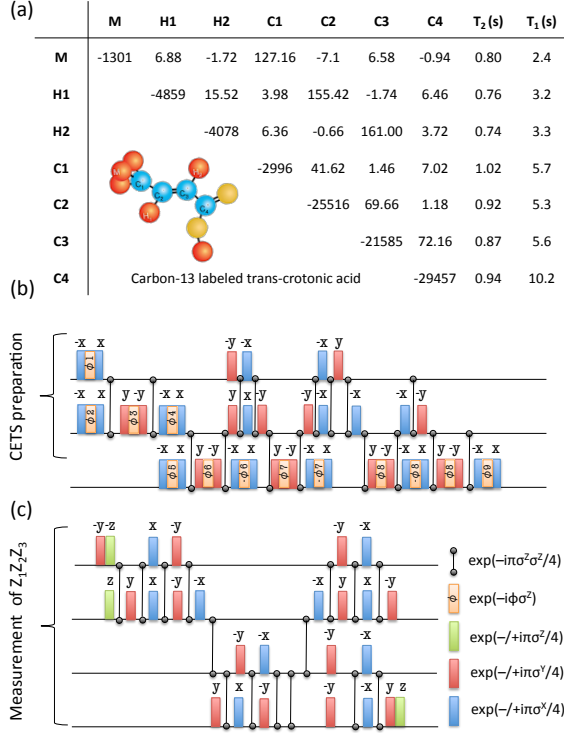


FIG. 2: Experimental protocol. (a) Hamiltonian parameters for the nuclear spins in carbon-13 labelled trans-crotonic acid, with the structure shown as the inset. The chemical shifts and J-coupling constants (in Hz) are listed on and above the diagonal in the table, respectively. The longitudinal and transversal relaxation times  $T_1$  and  $T_2$  measured by standard inversion recovery and Hahn echo pulse sequences are listed at right. The chemical shifts are given with respect to reference frequencies of 700.13 MHz (protons) and 176.05 MHz (carbons). The molecule provides seven qubits since the methyl group can be treated as a single qubit using a gradient-based subspace selection [22]. (b,c) Pulse sequences for preparing the CETS and measuring  $Z_1 Z_2 Z_3$  via the probe qubit, respectively, where refocusing pulses are not shown. The three carbons  $C_2$ ,  $C_3$  and  $C_4$  act as the CETS register qubits 1, 2 and 3, and  $C_1$  acts as the probe qubit. The rotation angles are determined by the angles in Fig. 1 are listed in the supplementary material.

the decay of their initial state  $00\sigma^z1111$ , where  $11$  denotes the identity operator (see supplementary material for details).

Since  $\sigma^z = 0 - 1$  with  $1 \equiv |1\rangle\langle 1|$ , the 64 peaks are divided into two antiphase multiplets corresponding to the two eigenstates of  $H_2$  (see supplementary materials). We may, for example, choose the group marked by the  $H_2$  state  $0$ . By adding the intensities of the 8 peaks marked by the state  $0_M 0_{H_1} 0_{H_2}$ ,  $\langle U_M \rangle$  is obtained, taking into account proper normalization relative to the initial pseudopure state  $\rho_s$ .

The experimental results are summarized as follows: the diagonal elements of the density matrix constructed

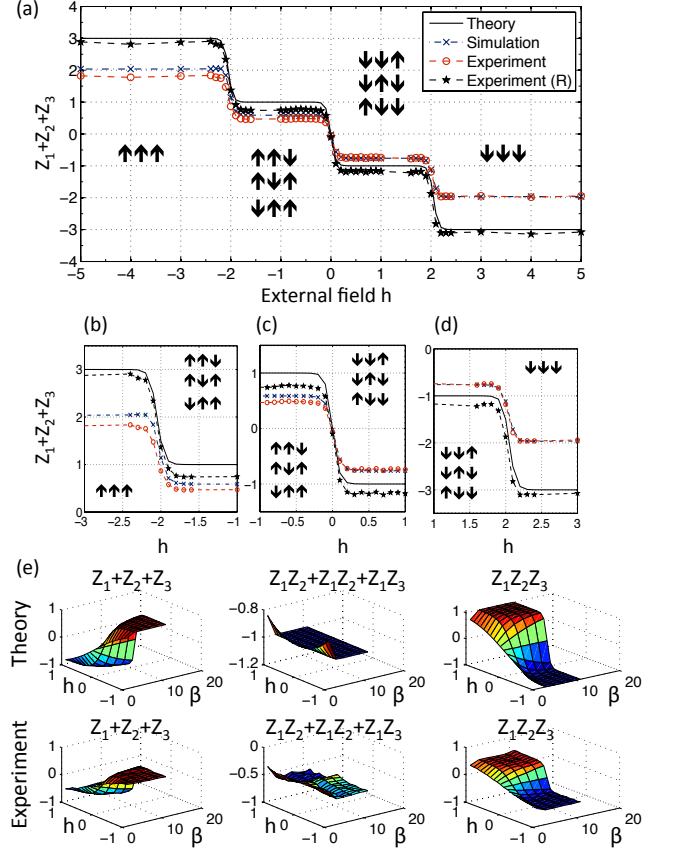


FIG. 3: Experimental measured magnetization and correlations. (a) Magnetization  $Z_1 + Z_2 + Z_3$  as a function of magnetic field  $h$  at low temperature,  $T = 1/11$ . The experimental data (“o”) is plotted together with numerical simulation results (“x”) that include effects of carbon  $T_2$  and proton  $T_1$ . The theoretical result is shown as the solid curve. The points labeled “Experiment (R)” are obtained from the experimental data by using a simple decoherence model to partially remove the effects of decoherence with no free parameters (described in the text). The sharp change show the phase transitions, and the regions around the critical points  $h = -2, 0, 2$  are enlarged as figures (b-d), respectively. (e) Surface plots for the total magnetization  $Z_1 + Z_2 + Z_3$ , correlations  $Z_1 Z_2 + Z_2 Z_3 + Z_1 Z_3$ , and  $Z_1 Z_2 Z_3$  in theory (top row) and measured in experiment (bottom row).

by the CETS are determined by measuring the full set of diagonal Pauli operators [see Eq. (5)] for a range of simulated temperatures  $T$  and external fields  $h$ . The experimental results are shown in Fig. 3. In Fig.3a, for a low temperature ( $\beta = 11$ ), the total magnetization  $Z_1 + Z_2 + Z_3$  of the frustrated magnet is probed for a range of the simulated field  $h$ . The raw experimental results are in good agreement with the numerical simulation which takes into the account the decoherence effects. By rescaling the total magnetization by a constant factor, which is equivalent to removing the isotropic errors [29] (see also supplementary material), the rescaled re-

sults agree much better with the theoretical predictions. In any case, it is clear that the magnetization changes in steps when the simulated magnetic field is varied from a large negative value ( $h = -5$ ) to a large positive value ( $h = 5$ ). The critical points for the crossovers are located at  $h = \pm 2$ , and 0, in agreement with the theoretical prediction shown in Fig. 1a. This is the result of the competition between the antiferromagnetic couplings and the external field applied to the frustrated magnet.

Apart from the total magnetization, the other correlation functions are probed systematically for a range of the simulated temperatures and external fields. The results are shown in Fig. 3e. From these data, we can construct the thermal state density matrix of the frustrated magnet (subject to the normalization condition  $\text{Tr}(\rho_{th}) = 1$ ):

$$\rho_{th} = \frac{1}{8} \mathbb{1} + \sum_i a_i Z_i + \sum_{j < k} b_{jk} Z_j Z_k + c Z_1 Z_2 Z_3, \quad (7)$$

where  $a_i \equiv \langle Z_i \rangle / 8$ ,  $b_{jk} \equiv \langle Z_j Z_k \rangle / 8$ , and  $c \equiv \langle Z_1 Z_2 Z_3 \rangle / 8$ . We ignore the imaginary parts of the elements, which are zero in theory, and less than 11% in the experimental data. With complete knowledge of the thermal density matrix  $\rho_{th}$ , we can determine all of the macroscopic thermodynamic observables for an ensemble of frustrated magnets. In this study, we are particularly interested in investigating a non-linear quantity, namely the entropy,

$$S = -\text{Tr}\{\rho_{th} \ln \rho_{th}\}, \quad (8)$$

and gauge how sensitive it is to experimental errors in  $\langle U_M \rangle$ .

Fig. 4a shows the experimental results for the entropy  $S$  as a function of the simulated magnetic field  $h$  in the low temperature regime ( $\beta = 11$ ). One finds that the sharp changes of  $S$  around  $h = \pm 2$  and 0 correspond to the crossovers, which have been observed in measurement of the total magnetization. Compared with the region of  $|h| > 2$ , the large values of  $S$  in the region  $|h| < 2$ , especially around  $h = 0$ , indicates the preference of antiferromagnetism which causes the frustration for the magnet. For the outer region  $|h| > 2$ , where the external field should be strong enough to polarize the magnet, the theoretical predictions of  $S$  should be zero. However, the experiment results, including the rescaled results, show non-zero values. This is due to the anisotropy of the measurement results taken from the three nuclear spins. The surface plots in Fig. 4b-d show the entropy as a function of  $h$  and  $\beta$  from theory (b), experiment (c), simulation (d), and the rescaled experimental results that partially remove decoherence effects (e). We see that the role of the temperature is to “wash out” the competition between the antiferromagnetic coupling and the external field. This is indicated by a transition near some value of the temperature ( $\beta = 3$ ), beyond which the variation of the simulated external field  $h$  no longer causes sharp crossovers.

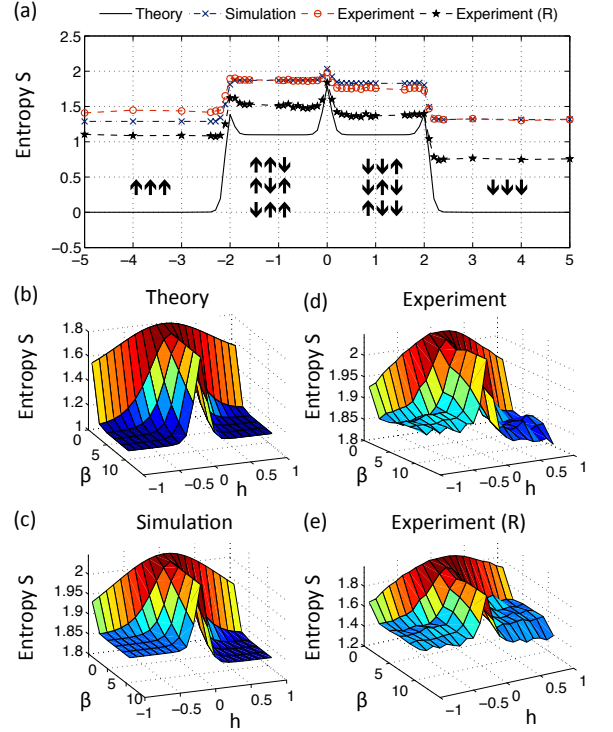


FIG. 4: (a) Entropy  $S$  as a function of magnetic field  $h$  at low temperature,  $\beta = 11$ . The experimental data (“o”) is plotted together with numerical simulation results (“x”) that include effects of carbon  $T_2$  and proton  $T_1$ . The theoretical result is shown as the solid curve. The sharp changes of  $S$  around  $h = \pm 2$  and 0 indicate the phase transitions. The points labeled “Experiment (R)” are obtained from the experimental data by using a simple decoherence model to partially remove the effects of decoherence with no free parameters (see SI). (b-e) Surface plots of entropy as a function of  $h$  and  $\beta$  from theory (b), experiment (c) and simulation (d). Modified experimental results that partially remove decoherence effects are shown in (e).

To summarize, the imperfection of the experimental results is mainly due to decoherence effects; the duration of the experiment ranges from 0.35-0.76 s, (see supplementary material for details), which is comparable with the  $T_2$  times of the nuclear spins. The simulated data, which take into account the nuclear  $T_2$  decay, closely match the experimental results. To a much lesser extent, inhomogeneities of the applied magnetic fields and imperfect pulses also contribute to the error. Partial recovery of the density matrix is possible for isotropic errors (see supplementary material), this allows us to rescale the magnetization to improve the agreement with the theoretical values (see Fig. 3). The anisotropic part of the error, however, cannot be removed, and significantly affects the experimental entropy results (see Fig. 4).

The phase kick-back method was chosen for readout to exploit the fact that all J-couplings are well resolved for spin  $C_1$ . For spins  $C_2$  and  $C_3$ , there is non-negligible

overlap between certain spectral peaks, which makes direct state tomography unreliable for certain states. Nonetheless, for certain simple states like  $|1111\rangle$  at  $\beta = 11$  and  $h = 5$ , state tomography through direct readout of all three spins can be performed reliably and compared to the phase kick-back results. The state fidelity measured in this fashion was close to the phase kick-back result, only differing by 0.4% (see Fig. 6 in supplementary information).

In conclusion, we employed a quantum information processor using nuclear spins to perform a digital quantum simulation of a geometrically frustrated magnet subject to a simulated magnetic field. We explored the phase diagram of this system for a range of temperatures and magnetic fields, and studied the competition between the antiferromagnetic couplings and the external field; the crossover points where the magnetic field quenches the frustration are correctly captured, and the overall experimental results are in good agreement with numerical simulations and theory.

## AUTHOR CONTRIBUTIONS

J.-F.Z. and J. B. designed the NMR experiments and simulations, which were carried out by J.-F.Z.; M.-H.Y. and A.A.-G. made the theoretical proposal and contributed to the analysis of results. R.L. and J. B. supervised the experiment. All authors contributed to the writing of the paper and discussed the experimental procedures and results.

## ACKNOWLEDGMENTS

We thank J. D. Whitfield for insightful discussions, and are grateful to the following funding sources: Croucher Foundation (M.H.Y); DARPA under the Young Faculty Award N66001-09-1-2101-DOD35CAP, the Camille and Henry Dreyfus Foundation, and the Sloan Foundation; Army Research Office under Contract No. W911NF-07-1-0304 (A.A.G.); CIFAR, SHARCNET and Quantum-Works (R.L.), and NSERC (J.-F. Z., R. L. and J. B.)

---

\* These authors contributed equally to this work.

- [1] Mezard. M., Parisi. G., Virasoro. M. A., *Spin glass theory and beyond* (World scientific, Teaneck, NJ, USA, 1987).
- [2] Feynman, R.P. Simulating physics with computers. *Int. J. Theor. Phys.* **21**, 467-488 (1982).
- [3] Peng, X., Du, J., Suter, D. Quantum phase transition of ground-state entanglement in a Heisenberg spin chain simulated in an NMR quantum computer. *Phys. Rev. A* **71**, 012307 (2005).
- [4] Friedenauer, A. et al. Simulating a quantum magnet with trapped ions. *Nature Phys.* **4**, 757-761 (2008).
- [5] Kim, K. et al. Quantum simulation of frustrated Ising spins with trapped ions. *Nature* **465**, 590-593 (2010).
- [6] Edwards, E. et al. Quantum simulation and phase diagram of the transverse-field Ising model with three atomic spins. *Phys. Rev. B* **82**, 060412 (2010).
- [7] Ma, X.-song et al. Quantum simulation of the wavefunction to probe frustrated Heisenberg spin systems. *Nature Phys.* **7**, 1-7(2011).
- [8] Struck, J. et al. Quantum simulation of frustrated magnetism in triangular optical lattices. *arXiv:1103.5944* (2011).
- [9] Buluta, I., Nori, F. Quantum simulators. *Science* (New York, N.Y.) **326**, 108-11 (2009).
- [10] Kassal, I. et al. Simulating chemistry using quantum computers. *Annu. Rev. Phys. Chem.* **62**, 185-207 (2011).
- [11] Mattis, D. C., and Swendsen, R. H., *Statistical Mechanics Made Simple, 2nd ed.* (World Scientific, Singapore, 2008).
- [12] Young, A.P., Knysh, S., Smelyanskiy, V. N., Size Dependence of the Minimum Excitation Gap in the Quantum Adiabatic Algorithm. *Phys. Rev. Lett.* **101**, 170503 (2008).
- [13] Nishimori, H., Wong, K. Statistical mechanics of image restoration and error-correcting codes. *Phys. Rev. E* **60**, 132-144 (1999).
- [14] Istrail, S. Statistical mechanics, three-dimensionality and NP-completeness: I. Universality of intracatability for the partition function of the Ising model across non-planar surfaces. *Proceedings of the thirty-second annual ACM symposium on Theory of computing* 87-96 (2000).
- [15] Temme, K. et al. Quantum Metropolis sampling. *Nature* **471**, 87-90 (2011).
- [16] Yung, M.-H., Aspuru-Guzik, A. A Quantum-Quantum Metropolis Algorithm. *arXiv:1011.1468* (2010)
- [17] Lidar, D., Biham, O. Simulating Ising spin glasses on a quantum computer. *Phys. Rev. E* **56**, 3661-3681(1997).
- [18] Yung, M.-H. et al. Simulation of classical thermal states on a quantum computer: A transfer-matrix approach. *Phys. Rev. A* **82**, 060302 (2010).
- [19] Winograd, E. a, Rozenberg, M.J., Chitra, R. Weak-coupling study of decoherence of a qubit in disordered magnetic environments. *Phys. Rev. B* **80**, 214429 (2009).
- [20] Lloyd, S. Universal Quantum Simulators. *Science* **273**, 1073-1078 (1996).
- [21] Kaye, P., Laflamme, R., Mosca, M. *An Introduction To Quantum Computing* (Oxford University Press, 2007).
- [22] Knill, E. et al. An algorithmic benchmark for quantum information processing. *Nature* **404**, 368-70 (2000).
- [23] Khaneja, N. et al. Optimal control of coupled spin dynamics: design of NMR pulse sequences by gradient ascent algorithms. *Journal of magnetic resonance. J. Magn. Reson.* **172**, 296-305 (2005).
- [24] Ryan, C. a et al. Liquid-state nuclear magnetic resonance as a testbed for developing quantum control methods. *Phys. Rev. A* **78**, 012328 (2008).
- [25] Maffei, P. et al. Slice selection in NMR imaging by use of the B<sub>1</sub> gradient along the axial direction of a saddle-shaped coil. *Journal of Magnetic Resonance* (1969) **95**, 382-386(1991).
- [26] Leskowitz, G., Mueller, L. State interrogation in nuclear magnetic resonance quantum-information processing. *Phys. Rev. A* **69**, 052302 (2004).
- [27] Chuang, I.L. et al. Bulk quantum computation with nuclear magnetic resonance: theory and experiment. *Proc.*

- R. Soc. Lond. A **454**, 447-467(1998).
- [28] Souza, A.M. et al. Experimental magic state distillation for fault-tolerant quantum computing. Nat. Commun. **2**, 169 (2011).
- [29] Yung, M.-H., under preparation.



## Supplementary information: Digital Quantum Simulation of the Statistical Mechanics of a Frustrated Magnet

### Quantum circuit construction for creating the CETS

For clarity, we re-write the Hamiltonian of the frustrated magnet as:

$$H = J(s_1 s_2 + s_2 s_3 + s_1 s_3) + h(s_1 + s_2 + s_3) \quad , \quad (9)$$

where  $s = \{0, 1\}$ , and  $Z|s\rangle = (-1)^s |s\rangle$ . To construct the quantum circuit diagram for creating the CETS of the frustrated magnet, we first consider the general property for the following controlled operation:

$$|s_1 s_2\rangle \otimes |0\rangle \rightarrow |s_1 s_2\rangle \otimes (\cos \theta |0\rangle + \sin \theta |1\rangle) \quad , \quad (10)$$

where

$$\cos \theta = \sqrt{e^{-\beta J(s_1 + s_2) - \beta h} / K} \quad (11)$$

and

$$\sin \theta = \sqrt{e^{+\beta J(s_1 + s_2) + \beta h} / K} \quad , \quad (12)$$

and

$$K \equiv e^{-\beta J(s_1 + s_2) - \beta h} + e^{+\beta J(s_1 + s_2) + \beta h} \quad . \quad (13)$$

Note that the numerators in Eq. (11) and Eq. (12) are chosen such that they give the correct weight of the Boltzmann factors. Now, one can show that

$$K = A e^{\beta b s_1 s_2} e^{\beta c (s_1 + s_2)} \quad , \quad (14)$$

where

$$\begin{aligned} A &= 2 \left( \sqrt{\cosh(2\beta J + \beta h) \cosh(2\beta J - \beta h) \cosh(\beta h)} \right)^{1/2} , \\ b &= \frac{1}{4\beta} \ln \left[ \frac{\cosh(2\beta J + \beta h) \cosh(2\beta J - \beta h)}{\cosh^2(\beta h)} \right] , \\ c &= \frac{1}{4\beta} \ln \left( \frac{\cosh(2\beta J + \beta h)}{\cosh(2\beta J - \beta h)} \right) . \end{aligned} \quad (15)$$

Combining these results, we can interpret the operation in Eq. (10) as the one that gives the correct Boltzmann factors to the terms involving the third qubit, but it will renormalize the first two qubits, according to Eq. (14).

This suggests that in order to prepare the three-qubit CETS, we will need to prepare the CETS for the first two qubits with respect to a Hamiltonian which takes into account the renormalization effect caused by the third qubit:

$$H = \tilde{J} s_1 s_2 + \tilde{h} (s_1 + s_2) \quad , \quad (16)$$

where

$$\tilde{J} \equiv J - b \quad , \quad (17)$$

and

$$\tilde{h} \equiv h - c \quad . \quad (18)$$

This can be achieved by the gates  $U_x$ ,  $U_y$  and  $U_z$  shown in the quantum circuit diagram Eq. (1)c. Their explicit forms are as follows:  $U_x \equiv R(\theta_x)$ ,  $U_y \equiv R(\theta_y)$ , and  $U_z \equiv R(\theta_z) R(\theta_y)^{-1}$ , where

$$R(\theta) = \begin{pmatrix} \cos \theta & -\sin \theta \\ \sin \theta & \cos \theta \end{pmatrix} \quad , \quad (19)$$

and

$$\cos \theta_x \equiv \sqrt{\frac{e^{-\beta(\tilde{h}-g)}}{2 \cosh \left[ \beta \left( \tilde{h} - g \right) \right]}} \quad , \quad (20)$$

and

$$\cos \theta_y \equiv \sqrt{\frac{e^{-\beta(\tilde{J}+\tilde{h})}}{2 \cosh \left[ \beta \left( \tilde{J} + \tilde{h} \right) \right]}} \quad , \quad (21)$$

and

$$\cos \theta_z \equiv \sqrt{\frac{e^{-\beta(-\tilde{J}+\tilde{h})}}{2 \cosh \left[ \beta \left( -\tilde{J} + \tilde{h} \right) \right]}} \quad . \quad (22)$$

Here

$$g = \frac{1}{2\beta} \ln \frac{\cosh(\beta \tilde{J} + \beta \tilde{h})}{\cosh(\beta \tilde{J} - \beta \tilde{h})} \quad . \quad (23)$$

The second part of the quantum circuit diagram implements the transformation Eq. (10), and involves the gates  $U_0$ ,  $U_1$  and  $U_2$ . Their explicit forms are given by:  $U_0 \equiv R(\theta_0)$ ,  $U_1 \equiv R(\theta_1) R(\theta_0)^{-1}$ , and  $U_2 \equiv R(\theta_2) T^{-1}(\theta_1, \theta_0)$ , where  $T(\theta_1, \theta_0) \equiv R(\theta_1) R(\theta_0)^{-1} R(\theta_1)$ ,

$$\cos \theta_0 \equiv \sqrt{\frac{e^{-(\beta 2J + \beta h)}}{2 \cosh(\beta 2J + \beta h)}} \quad , \quad (24)$$

and

$$\cos \theta_1 \equiv \sqrt{\frac{e^{-\beta h}}{2 \cosh(\beta h)}} \quad , \quad (25)$$

and

$$\cos \theta_2 \equiv \sqrt{\frac{e^{\beta 2J - \beta h}}{2 \cosh(\beta 2J - \beta h)}} \quad . \quad (26)$$



### Partial recovery from isotropic noise

We applied an empirical transformation of the measurement results to partially remove decoherence errors. There is no rigorous proof that this transformation will work for all circumstances, however, there are reasonable motivations for it. In this experiment, all of the observables  $\langle U_M \rangle$  are obtained by measuring the coherence of the probe qubit (see Eq. (4)). For the moment, if we only take into account the  $T_2$  decay of the probe qubit, then all of the measured values should be smaller than the actual value by a value roughly equal to  $\eta \equiv e^{-\tau/T_2}$ . Here  $\tau$  is the evolution time, and we assume it is the same for all of the measurements. This assumption is equivalent to saying that the prepared CETS  $|\Psi_\beta\rangle$  is subject to the depolarizing channel:

$$\rho_\varepsilon \equiv \varepsilon(\rho_c) = (1 - \eta) \frac{I}{D} + \eta \rho_c \quad , \quad (27)$$

where  $\rho_c \equiv |\Psi_\beta\rangle \langle \Psi_\beta|$ , and  $D = 8$  is the dimension of the CETS. In the ideal case where  $\eta$  is known, the CETS can be perfectly recovered from  $\rho_\varepsilon$  by the following transformation:

$$\rho_c = \left( \rho_\varepsilon - \frac{I}{D} \right) \times \frac{1}{\eta} + \frac{I}{D} \quad . \quad (28)$$

Or equivalently, we may simply multiply all of the observables by the factor  $\eta$ .

In reality, a depolarizing channel as a noise model is a pure assumption, and it is almost impossible to determine the exact value of  $\eta$ , e.g. in the case where the decay rate for each observable may be different from the others. Nonetheless, partial recovery from the noise is possible when the decay rates are roughly the same, and we may estimate  $\eta$  in an average sense. To see this, consider the trace-preserving transformation:

$$\left( \rho_\varepsilon - \frac{I}{D} \right) \times \frac{1}{\lambda} + \frac{I}{D} = \frac{\eta}{\lambda} \rho_c + \left( 1 - \frac{\eta}{\lambda} \right) \frac{I}{D} = \rho' \quad (29)$$

where  $\lambda$  is assumed to be close to  $\eta$ . It is easy to check that this transformation is not positive. However, as long as  $\lambda$  is close to  $\eta$ , the rescaled state  $\rho'$  is approximately equal to  $\rho_c$ , i.e., the original CETS.

In fact, for the depolarizing channel applied to a pure state, i.e.,  $\text{Tr}(\rho_c^2) = 1$ , a systematic estimation for  $\eta$  is possible. To see this, consider taking the trace of the square of  $\rho_\varepsilon$  in Eq. (27), we find that

$$\eta = \sqrt{\frac{\text{Tr}(\rho_\varepsilon^2) - 1/D}{1 - 1/D}} \quad . \quad (30)$$

When  $D$  is much larger than 1, we have the approximation

$$\eta \approx \sqrt{\text{Tr}(\rho_\varepsilon^2)} \quad . \quad (31)$$

If we take this correction to the density matrix to calculate the fidelity with the  $|\Psi_\beta\rangle$  CETS, the result, in the limit  $D \gg 1$ , is the same as that of the projection between them:

$$P \equiv \frac{\langle \Psi_\beta | \rho_\varepsilon | \Psi_\beta \rangle}{\sqrt{\text{Tr}(\rho_\varepsilon^2)}} \quad . \quad (32)$$

Although, in theory, Eq. (30) is an exact expression for  $\eta$ , in practice, it can easily cause the final density matrix to have negative eigenvalues. Empirically, the approximation  $\eta \approx \sqrt{\text{Tr}(\rho_\varepsilon^2)}$  works much better. In this experiment, we chose  $\eta = 0.6316$ , which is equal to the square root of the purity of the measured CETS at  $\beta = 11$  and  $h = 5$ . With a single fitting parameter, the total magnetizations for all of the states are rescaled to values much closer to the theoretical values, as shown in Fig. 3a-d.

The term “isotropic error” in the main text refers to the part of the error generated by the uniform part of the decoherence. To make the statement more quantitative, as an example, consider two observables which suffer from two different dephasing rates  $\gamma_1$  and  $\gamma_2$ . The isotropic error can be quantified by defining the mean value  $\gamma_m \equiv (\gamma_1 + \gamma_2)/2$ . By rescaling the factor  $e^{\gamma_m t}$  to both observables, the effective decay rate becomes the anisotropic error rates  $\gamma_1 - \gamma_m$  and  $\gamma_2 - \gamma_m$ , which is zero when  $\gamma_1 = \gamma_2$ .

Lastly, we emphasize again that this decoherence model is a pure assumption, and to motivate the use of it, we considered only the dephasing of the probe qubit. In reality, there are also decoherence channels for the other qubits. On the other hand, the depolarizing noise model is a useful approximation when we consider that the applied pulse sequences may randomize the noise to some extent. In the limit that we apply a large number of random operations uniformly drawn from the Clifford gates, we would in fact get exactly a uniform depolarizing channel (See, e.g., C A Ryan et al 2009 New J. Phys. 11 013034).

### $T_1$ relaxation of the proton spins

In implementing the pseudopure state,  $\rho_s$  starts from the state  $\sigma^z \mathbb{1} \mathbb{1} \mathbb{1} \mathbb{1} \mathbb{1} \mathbb{1}$ .

In the experiment, the proton spins  $M$ ,  $H_1$  and  $H_2$  are prepared in the state  $\mathbf{00}\sigma^z$ . We measured the decay of the state  $\mathbf{00}\sigma^z \mathbb{1} \mathbb{1} \mathbb{1} \mathbb{1}$  in order to estimate the effect of the protons'  $T_1$  relaxation process on the measurement of the CETS. The state  $\mathbf{00}\sigma^z \mathbb{1} \mathbb{1} \mathbb{1} \mathbb{1}$  is prepared from  $\rho_s = \sigma^z \mathbb{1} \mathbb{1} \mathbb{1} \mathbb{1} \mathbb{1} \mathbb{1}$  through phase cycling. After a delay time, a  $\pi/2$  readout pulse for  $H_2$  is applied. The intensity of the signal against the delay time is shown in Fig. 5, with a fit yielding a relaxation time of 2.95 s.

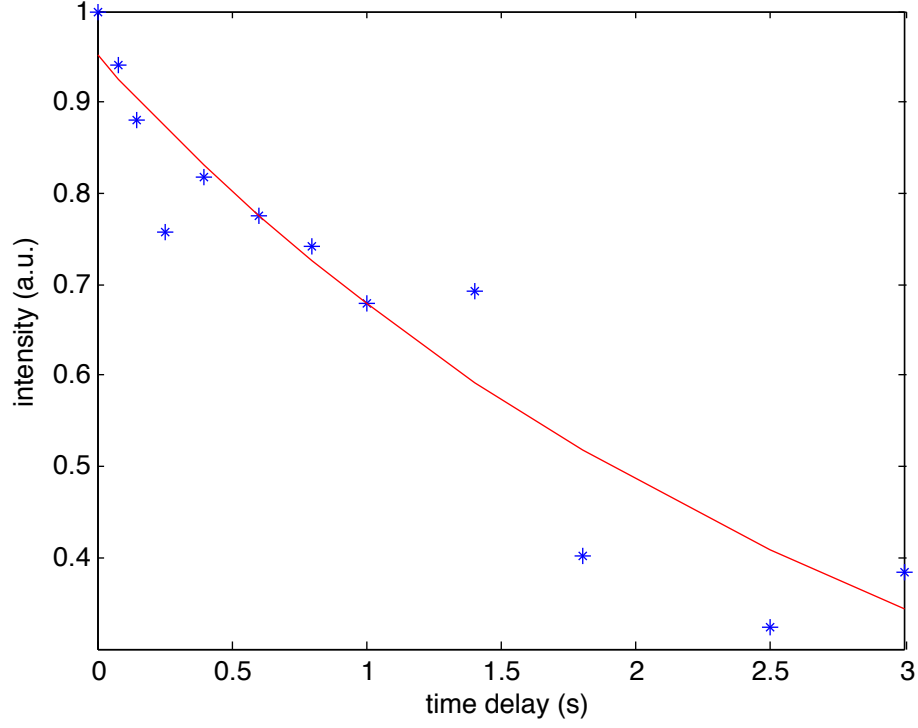


FIG. 5: The decay of the  $H_2$  signal obtained by a  $\pi/2$  readout pulse to the state  $00\sigma^z 11111$ . The experimental data are denoted by \*, and the fitting result is shown as the solid curve.

#### Supplementary data

The supplementary figures are shown below. They include a table summarizing the experimental durations

for various measurement observables, the spectra of the probe qubit, and selected measurement results not included in the main text.

Measurement	Experiment duration (s)	Theoretical value	Experimentally measured value
$\langle Z_1 \rangle$	0.35	-1/3	-0.2497
$\langle Z_2 \rangle$	0.46	-1/3	-0.1208
$\langle Z_3 \rangle$	0.57	-1/3	-0.2564
$\langle Z_1 Z_2 \rangle$	0.62	-1/3	-0.1335
$\langle Z_2 Z_3 \rangle$	0.58	-1/3	-0.3377
$\langle Z_1 Z_3 \rangle$	0.76	-1/3	-0.1549
$\langle Z_1 Z_2 Z_3 \rangle$	0.59	1	0.5110
$\langle X_1 \rangle$	0.37	0	0.2007
$\langle X_2 \rangle$	0.49	0	0.0743
$\langle X_3 \rangle$	0.63	0	0.0154
$\langle Y_1 \rangle$	0.37	0	-0.1261
$\langle Y_2 \rangle$	0.49	0	-0.1375
$\langle Y_3 \rangle$	0.63	0	-0.1769

TABLE I: Experimental parameters for estimating errors in implementation. Experiment duration for measuring  $U_M$  includes the preparation of CETS, which takes 0.33 s. The theoretical and experimental data correspond to  $T = 1/11$  and  $h = 1$ . The differences in the errors in for  $U_M$  give rise to the anisotropic part of the error in the reconstructed density matrix, which cannot be removed by the empirical transformation described above.

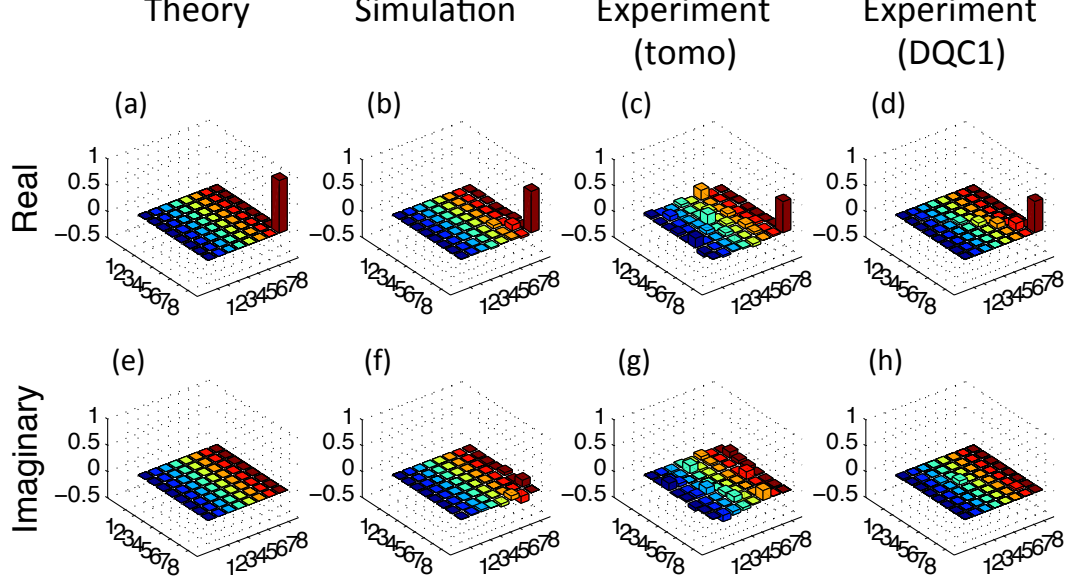


FIG. 6: Density matrices for  $T = 1/11$  and  $h = 5$ . From left to right, the four columns show the results in theory, by simulation (including  $T_2$ ), in experiment by full state tomography [26], and in experiment using the phase kick-back readout. The top and bottom rows show the real and imaginary parts, respectively. Compared with the theoretical result, the state fidelities from the simulation, state tomography and phase kick-back method are 79.8%, 60.2% and 59.8%, respectively.

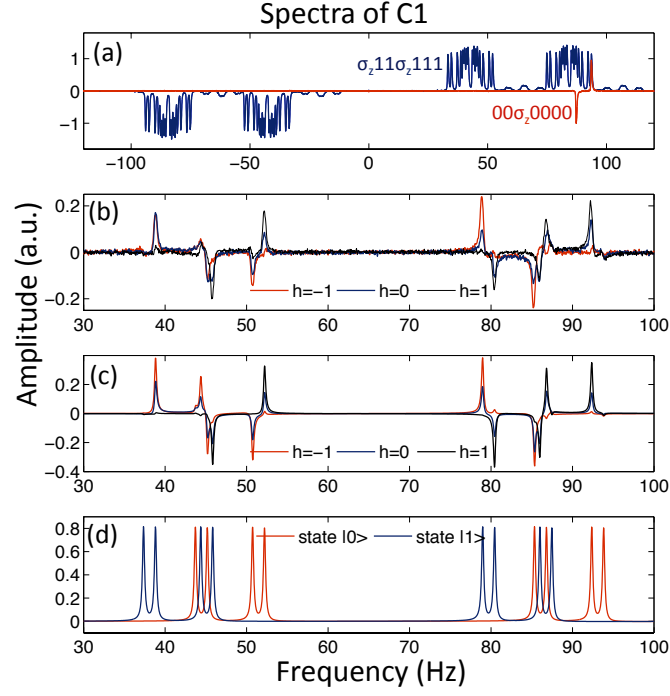


FIG. 7: (a) Spectra of  $C_1$  obtained by  $\pi/2$  readout pulses when the system is in the labelled pseudo-pure state  $\rho_s = 00\sigma_z 0000$  (red) and reference state  $\sigma_z \mathbb{1} \mathbb{1} \sigma_z \mathbb{1} \mathbb{1} \mathbb{1}$  (blue), respectively. The vertical axes have the same scaling (arbitrary units). (b,c) NMR spectra of  $C_1$  for measuring  $\langle Z_1 Z_2 Z_3 \rangle$  in experiment (b) and by simulation that includes  $T_2$  effects (c), with  $\beta = 5$ ,  $h = -1$  (red), 0 (blue), and 1 (black). In each spectrum, only the peaks marked by  $M$  in state  $|0\rangle$  are shown, because the peaks marked by  $M$  in state  $|1\rangle$  are too weak to attribute observable signals). (d) For reference, simulated spectra of  $C_1$  marked by spin  $H_2$  in state  $|0\rangle$  (dashed) and  $|1\rangle$  (solid) are shown (with  $C_2$ - $C_4$  in the state  $\mathbb{1}^{\otimes 3}$ ).

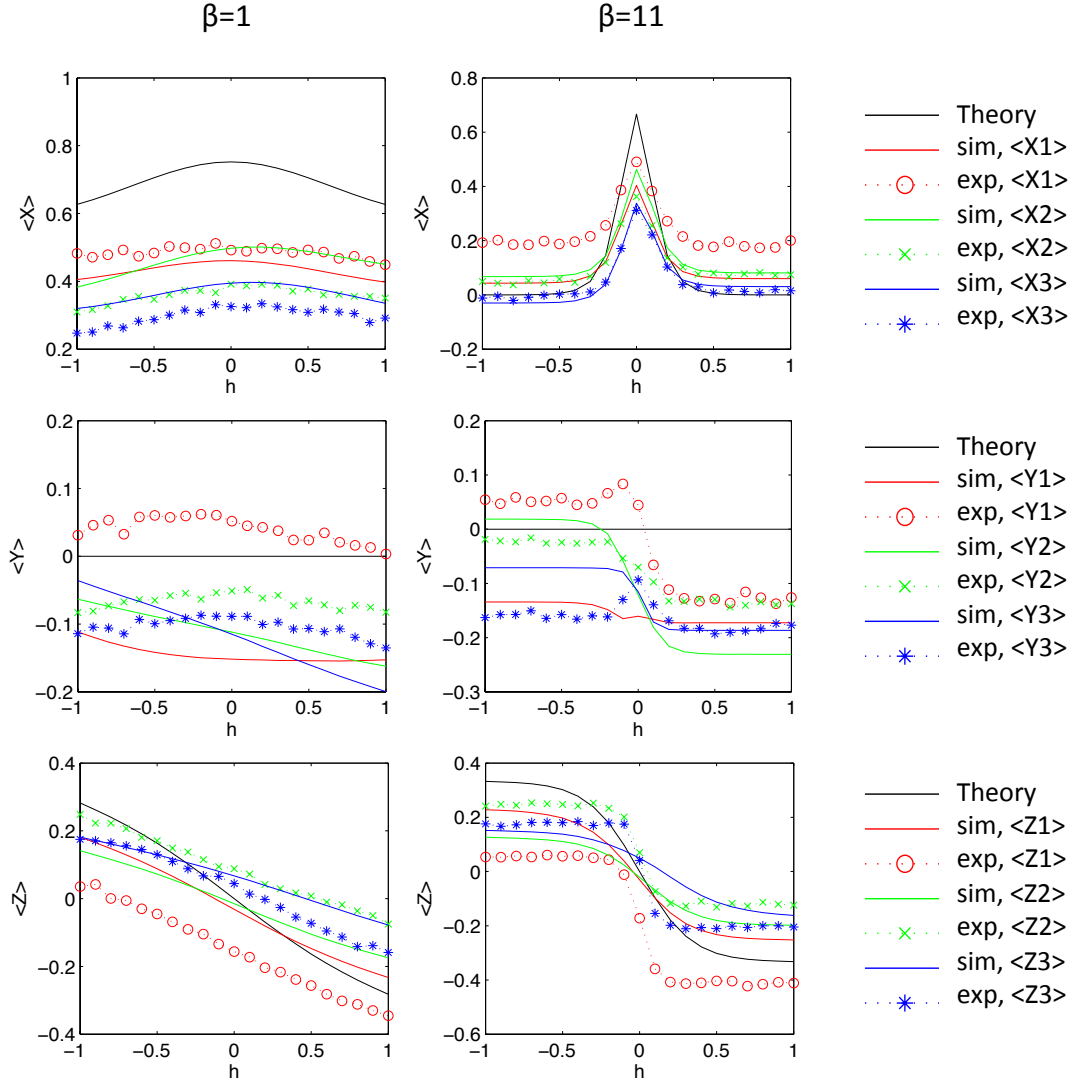


FIG. 8: Measurement results of  $\langle X \rangle$ ,  $\langle Y \rangle$  and  $\langle Z \rangle$  for the high-temperature limit  $\beta = 1$  (left) and the low-temperature limit  $\beta = 11$  (right).